In Situ Detection of Iron in Oxidation States ≥ IV in Cobalt-Iron Oxyhydroxide Reconstructed during Oxygen Evolution Reaction

Lukas Reith, Jan Niklas Hausmann, Stefan Mebs, Indranil Mondal, Holger Dau,* Matthias Driess,* and Prashanth W. Menezes*

Cobalt-iron oxyhydroxides (CoFeOOH$_x$) are among the most active catalysts for the oxygen evolution reaction (OER). However, their redox behavior and the electronic and chemical structure of their active sites are still ambiguous. To shed more light on this, the complete and rapid reconstruction of four helical cobalt-iron borophosphates with different Co:Fe ratios into disordered cobalt-iron oxyhydroxides can be achieved, which are electrolyte-penetrable and thus most transition metal sites can potentially participate in the OER. To track the redox behavior and to identify the active structure, quasi in situ X-ray absorption spectroscopy is applied. Iron in high oxidation states ≥ IV (Fe^{4+}) and its substantial redox behavior with an average oxidation state of around 2.8 to above 3.2 is detected. Furthermore, a 6% contraction of the Fe-O bond length compared to Fe^{3+}OOH references is observed during OER and a strong distortion of the [MO$_6$] octahedra is identified. It is hypothesized that this bond contraction is caused by the presence of oxyl radicals and that di-μ-oxyl radical bridged cobalt-iron centers are the active sites. It is anticipated that the detailed electronic and structural description can substantially contribute to the debate on the nature of the active site in bimetallic iron-containing OER catalysts.

L. Reith, J. N. Hausmann, I. Mondal, M. Driess, P. W. Menezes
Department of Chemistry
Metalorganics and Inorganic Materials
Technische Universität Berlin
Straße des 17 Juni 135, Sekr. C2, 10623 Berlin, Germany
E-mail: matthias.driess@tu-berlin.de;
prashanth.menezes@mailbox.tu-berlin.de
S. Mebs, H. Dau
Fachbereich Physik
Freie Universität Berlin
Arnimallee 14, 14195 Berlin, Germany
E-mail: holger.dau@fu-berlin.de
P. W. Menezes
Materials Chemistry Group for Thin Film Catalysis – CatLab
Helmholtz-Zentrum Berlin für Materialien und Energie
Albert-Einstein-Str. 15, 12489 Berlin, Germany
E-mail: prashanth.menezes@helmholtz-berlin.de

1. Introduction

A future sustainable energy economy and chemical industry based on wind and sun energy require effective electrocatalytic reduction reactions of abundant small molecules (e.g., water or carbon dioxide) for the formation of fuels and commodity chemicals (e.g., hydrogen, hydrocarbons, or alcohols).[1–5] For these reduction reactions, electrons and protons are required, which can only be provided on large scale by the kinetically demanding electrocatalytic oxygen evolution reaction (OER).[6–8] During the OER, water is oxidized and its O–H bonds are broken, which requires severe reaction conditions. During alkaline OER (aqueous potassium hydroxide electrolyte),[9] these severe conditions reconstruct non-noble-metal-based (Fe, Co, Ni) precatalysts into (partially) deprotonated layered oxyhydroxide structures that have been shown to intercalate potassium or carbonate (formed from CO$_2$ in the air) into their structures. In this report, we will call these layered double hydroxide-related structures oxyhydroxides, even though they could also be named oxides, due to their deprotonation.[10,11] To achieve high catalytic activities, these oxyhydroxides require iron sites.[12–14] However, monometallic oxyhydroxide suffers from poor electron conductivity and chemical stability.[14–16] Both disadvantages can be overcome by incorporating iron into cobalt- or nickel-based oxyhydroxides making the resulting bimetallic nickel-iron or cobalt-iron phases the most promising OER catalysts.[12–14]

The explanation for the strongly increased activity of cobalt and iron phases through iron incorporation is strongly debated.[17] For example, it has been proposed that i) iron is the active site and cobalt or nickel mainly provides a stabilizing and conducting matrix,[16–18] ii) iron modifies the structural and electronic properties of the nickel or cobalt sites, which drive catalysis,[19] and iii) bimetallic di-μ$_2$-oxo-bridged sites cooperatively catalyze the OER.[10,20] A clear indication of the electronic coupling of iron and cobalt/nickel is the anodic shift of the potentiometric (Co/Ni)^{II} oxidation peaks.[13,21,22] For cobalt- and nickel-based systems with and without iron incorporation, Ni^{IV} and Co^{IV} species have often been detected through in situ

measurements at OER potentials.[23–26] Because the oxo anion is redox noninnocent, these highly oxidized species might be best described as $M^{(3+\delta)+}$-$O^{(2-\delta)-}$ involving an electrophilic oxygen species, driving the required oxygen redox processes.[27–29] Compared to this rich redox activity involving $(Co/Ni)^{II/III/IV}$, iron has often been observed to remain in the oxidation state +3.[23,24,26] Nevertheless, iron in oxidation states above +3 has been proposed as a crucial OER catalysis intermediate.[30–34] These highly oxidized iron species might be significantly harder to detect, as they rapidly react with water driving efficiently the OER, and, in contrast to $(Ni/Co)^{IV}$, the Fe^{III} oxidation might be rate limiting and not a consecutive reaction step.[23,35,36] Thus, the highly oxidized iron concentration remains minute.

While the redox behavior of nickel-iron phases has been investigated intensively, only a few in situ spectroelectrochemical studies for cobalt-iron phases dealing with redox behavior and structural evolution exist.[17,30,31,37–40] In analogy to nickel-iron systems, the redox peaks of cobalt-iron phases have often been assigned to changes in the cobalt oxidation state, and iron is assumed to be redox inactive.[13,41–44] The reported cobalt-iron spectroelectrochemical studies come with contradicting results.[17] For example, Boettcher and co-workers observed a 0.7 eV shift of the X-ray absorption near edge structure (XANES) for the Fe K-edge comparing a sample at a pre-OER potential to one at an OER potential,[40] while Yeo and co-workers found no shift in the Fe K-edge,[38] as has often been observed for nickel-iron systems as well.[23] Additionally, the iron content resulting in the highest OER activity was found to be either around 50% or 25%.[13,45,46] These different observations are most likely caused by slight structural variations of the investigated cobalt-iron oxyhydroxide phases resulting from different synthetic protocols.

The previous spectroelectrochemical studies used $Co_xFe_{x-1}O_yH_z$ precursors.[37,38,40] Recently, it has been discovered that the reconstruction of precatalysts with leaching anions can lead to unordered oxyhydroxide phases.[11,25,47,48] These phases share the same short-range order (layers of edge-sharing [MO_6]-octahedra) like their crystalline counterparts but comprise smaller layers that stack in an unordered way.[25,48] These variations in the long-range order result in more catalytically active edge sites and an electrolyte penetrability enabling the catalyst bulk to participate in the OER.[25,48] We have recently discovered that helical borophosphates with channels containing strands of hydrate and coordinated water molecules are excellent precatalysts and lead to the formation of transition-metal oxyhydroxides that outperform those formed from simple (hydr)oxide

materials in terms of catalytic activity and stability.[49–52] Furthermore, Song and co-workers have shown that the reconstruction of such phases can be accelerated by ball milling leading to a complete transformation into oxyhydroxide phases.[52]

Herein, we used a mild hydrothermal approach to synthesize helical lithium $Fe_{1-x}Co_x$ borophosphates with different ratios for the first time and subsequently reduced the particle size by high-energy ball-milling (**Scheme 1**). The obtained helical $LiFe_{1-x}Co_x$ borophosphates particles were investigated for their electrocatalytic properties towards OER by using a wide variety of electrochemical and analytical in situ and ex situ techniques. Quasi in situ X-ray absorption spectroscopy (XAS) was applied to investigate the electronic and structural behavior of the active phase, demonstrating redox-active Fe with oxidation states higher than three and distorted [MO_6] octahedra.[34]

2. Results

2.1. Composition, Structure, and Morphology

The $LiFe_{1-x}Co_x(H_2O)_2[BP_2O_8]\cdot H_2O$ starting material ($Fe_{1-x}Co_xBPO$) was prepared via a mild hydrothermal synthesis method (see Experimental Section).[50] **Figure 1**a shows the powder X-ray diffraction (PXRD) pattern of previously reported $LiCo(H_2O)_2[BP_2O_8]\cdot H_2O$ (CoBPO),[50] which is used throughout this study for comparison. All $Fe_{1-x}Co_xBPO$ samples display the same pattern and share the same crystal structure as the helical CoBPO (Figure 1b). Adding iron to CoBPO results in a shift towards slightly lower angles, consistent with an expansion of the unit cell.[53] They crystallize in the space groups $P6_122$ (no. 178) and $P6_522$ (no. 179)).[54] The formed helices are "left-handed" (6_5) or "right-handed" (6_1), consisting of $^1_\infty[BP_2O_8]^{3-}$ chains formed by corner-shared alternating phosphate and borate tetrahedra. The $MO_4(OH_2)_2$ octahedra (M = Co, Fe) are interconnected with $^1_\infty[BP_2O_8]^{3-}$ helices along the [001] plane. The Li-ions are located in free threads of helices and are irregularly surrounded by oxygen anions. The crystal water forms hydrogen bonds to maintain structural stability.[50] The elemental composition was quantified by inductively coupled plasma optical emission spectrometry (ICP-OES, Table S1, Supporting Information) and confirmed the stoichiometries expected for helical borophosphates. In the hydrothermal synthesis, the Fe:Co precursor ratios were 1:3, 1:1, and 3:1, which resulted in final Fe:Co ratios of 0.33:0.67, 0.55:0.45, and 0.82:0.18, respectively, indicating that iron reacts slightly faster
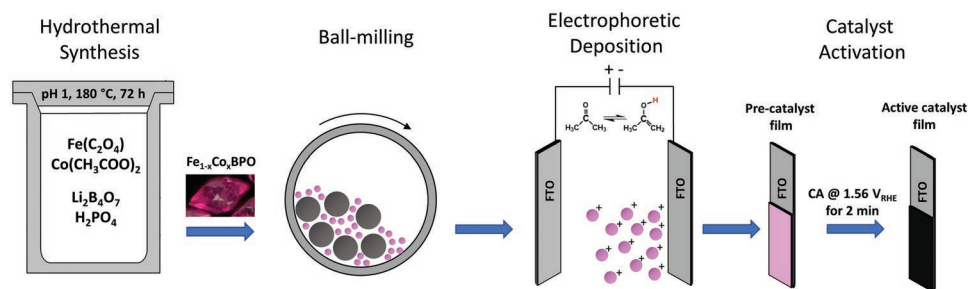
Scheme 1. Experimental procedure for the synthesis, ball-milling, electrophoretic deposition, and electrochemical activation process of the $Fe_{1-x}Co_xBPO$ samples.
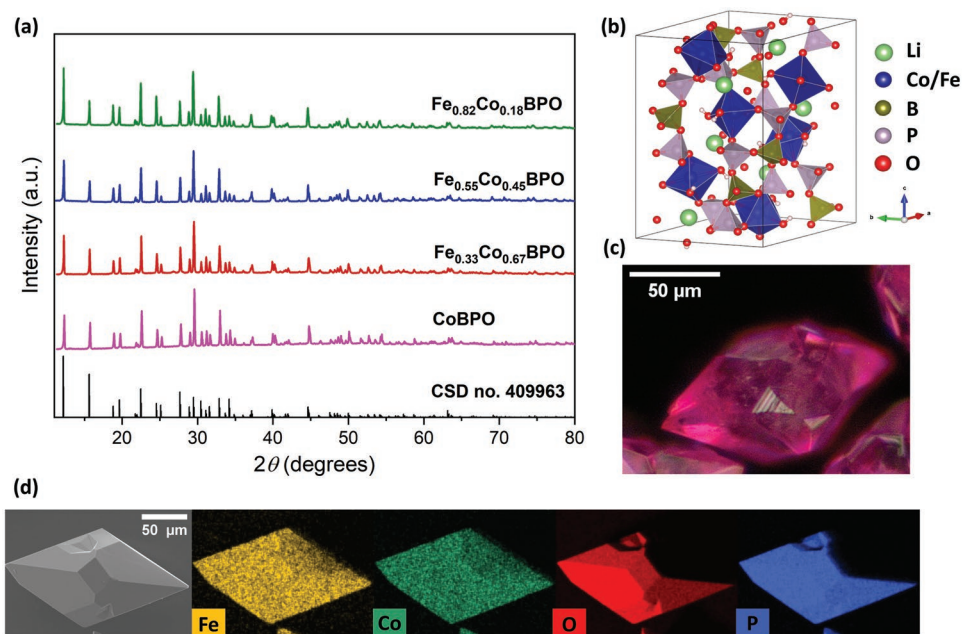
Figure 1. Structural and morphological data of the as-prepared helical LiFe$_{1-x}$Co$_x$ borophosphates (Fe$_{1-x}$Co$_x$BPO). a) Comparison of the PXRD patterns of the powder samples measured with Cu Kα radiation. The pattern of CSD no. 409963 was shown as a reference. b) Crystal structure of the helical LiFe$_{1-x}$Co$_x$ borophosphate, c) optical microscope image of a typical crystal (Fe$_{0.55}$Co$_{0.45}$BPO) obtained after synthesis. d) SEM/EDX mapping of Fe$_{0.55}$Co$_{0.45}$BPO showing the elemental distribution. Depending on the element-specific X-ray energy, the EDX surface sensitivity changes, explaining why the top right edge cannot be seen for oxygen and phosphorus.

than cobalt towards the borophosphate formation. Herein, these samples are named according to their composition Fe$_{0.33}$Co$_{0.67}$BPO, Fe$_{0.55}$Co$_{0.45}$BPO, and Fe$_{0.82}$Co$_{0.18}$BPO.

Optical and scanning electron microscopy (SEM) in Figure 1c and Figures S1 and S2, Supporting Information shows the pink single crystals from Fe$_{0.55}$Co$_{0.45}$BPO with a smooth surface and hexagonal bipyramidal shape typical for all Fe$_{1-x}$Co$_x$BPO samples.[55] Furthermore, SEM images with energy-dispersive X-ray (EDX) spectroscopy in Figure 1d and Figures S3 and S4, Supporting Information display a homogenous distribution of Fe, Co, O, and P throughout the 150 μm large single crystals and the Fe-Co EDX spectra quantification (Figure S5, Supporting Information) confirms the ICP-OES results (Table S1, Supporting Information). These results reveal that pure Fe$_{1-x}$Co$_x$BPO crystals were formed, instead of separate LiFe(H$_2$O)$_2$[BP$_2$O$_8$]·H$_2$O and CoBPO crystals.

The large particle size was reduced through ball-milling to increase the surface area, and facilitate the fabrication of catalyst films on the electrode via binder-free electrophoretic deposition (EPD).[52] The PXRD, XANES, extended X-ray absorption fine structure (EXAFS), and SEM-EDX of CoBPO after ball-milling and deposited on FTO (Figures S6–S13, Supporting Information), as well as ICP-OES results (Table S1, Supporting Information), show that there are no structural or chemical changes, as subtle amorphization is possible for such materials with high-energy ball-milling for long times.[52]

2.2. Electrochemical OER Performance

For electrochemical measurements, the ball-milled samples were deposited on fluorine-doped tin oxide (FTO) electrodes via EPD (loading 0.7 mg cm^{-2}). Before running any electrochemical test procedures, 2 min chronoamperometry (CA) at 1.56 V versus the reversible hydrogen electrode (V$_{RHE}$) was performed resulting in an immediate color change from (light) pink/gray to black/brown, shown in **Figure 2**a and Scheme S1, Supporting Information, indicating the reconstruction of the borophosphate precatalysts.[55,56] The CA current response at 1.56 V$_{RHE}$ shown in Figure 2b is large at the beginning and then sharply decreases, with a subsequent increase, until a stable current is reached. We assign the initial large current mainly to catalysts oxidation/reconstruction to oxyhydroxides consistent with the observed color change and previous reports.[25,57] The stable current after the catalyst oxidation is ascribed to the OER, revealing that Fe$_{0.33}$Co$_{0.67}$BPO and Fe$_{0.55}$Co$_{0.45}$BPO are the most OER-active. All catalysts were activated by this process.

The cyclic voltammograms (CV) of Figure 2c show that the 1st redox feature, the Co$^{II/III}$ wave, undergoes an anodic shift with increasing Fe content, showing that Co and Fe strongly interact. In contrast to nickel-iron-based materials, the addition of iron into the cobalt structure does not substantially reduce the reduction wave integral. This is especially interesting, as the Fe$_{0.55}$Co$_{0.45}$BPO contains less than 50% cobalt compared to the CoBPO one. Thus, either the redox activity per cobalt site almost doubled or iron itself participates in the redox process.
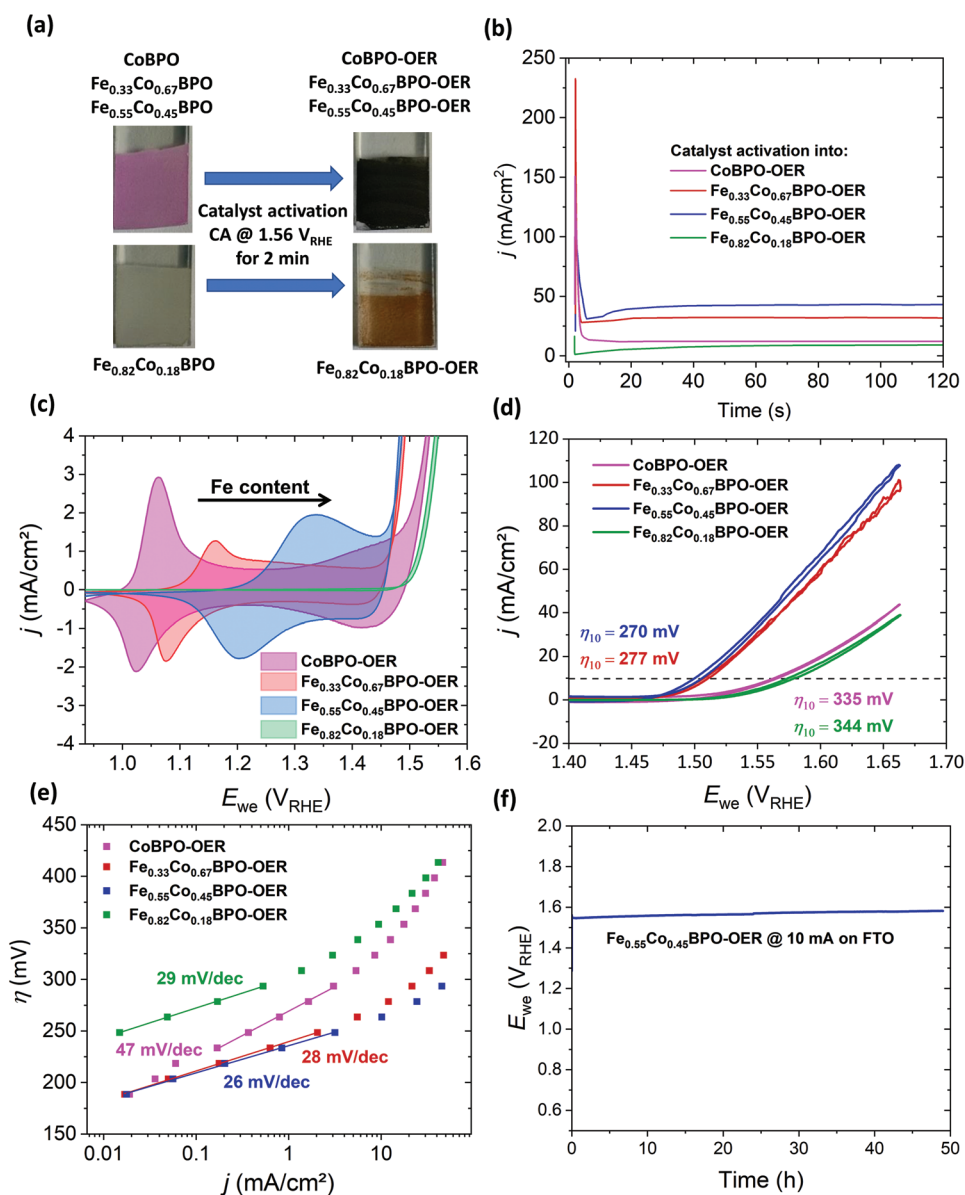
Figure 2. Electrochemical performance of the $Fe_{1-x}Co_xBPO$ (cobalt-iron oxyhydroxides) samples for OER using a three-electrode setup on FTO with a loading of 0.7 mg cm^{-2}. All measurements have been *iR*-corrected. Before the measurements (c–f) were performed, the samples were reconstructed into cobalt-iron oxyhydroxides by measurement (b). a) Catalyst activation process on FTO electrodes with deposited catalyst before (left) and after (right) CA at 1.56 V$_{RHE}$ for 2 min. b) CA curves for catalyst activation. c,d) CV curves of the samples showing the reversible redox features and the active OER region, respectively. e) The Tafel slopes obtained at steady-state measurements. f) Long-term stability test via CP at 10 mA cm^{-2}.

Furthermore, in contrast to the cobalt-rich materials, the sample with the highest amount of Fe ($Fe_{0.82}Co_{0.18}BPO$) does not show any significant redox peaks, which is typical for iron-rich phases which suffer from insufficient electron conductivity.[16,45]

In Figure 2d, the overpotentials of the catalysts at 10 mA cm^{-2} (η_{10}) are shown. $Fe_{0.82}Co_{0.18}BPO$ and CoBPO exhibit similar activities with η_{10} = 344 mV and η_{10} = 335 mV, respectively. Remarkably, $Fe_{0.33}Co_{0.67}BPO$ and $Fe_{0.55}Co_{0.45}BPO$, with η_{10} = 277 mV and η_{10} = 270 mV, respectively, are substantially more active, which is competitive with current literature on flat one-sided substrates.[58–60] Furthermore, we deposited several different oxidic mono- and bimetallic materials (e.g.,

[NiFe/Ni/Co/CoNi]OOH, Co_3O_4...) on FTO and tested their activity under identical conditions revealing a superior activity of the herein obtained $Fe_{0.55}Co_{0.45}BPO$ (see Figure S14, Supporting Information).

The kinetics of the catalysts were investigated by Tafel slopes (Figure 2e) measured by the steady-state method with *iR* correction.[61] To obtain information free of mass transport or surface coverage limitations the slopes have been measured at low current densities. The cobalt- and iron-containing oxyhydroxides display low Tafel slopes with comparable values of 29, 28, and 26 mV dec^{-1} for $Fe_{0.82}Co_{0.18}BPO$, $Fe_{0.33}Co_{0.67}BPO$, and $Fe_{0.55}Co_{0.45}BPO$, respectively. This is close to reported
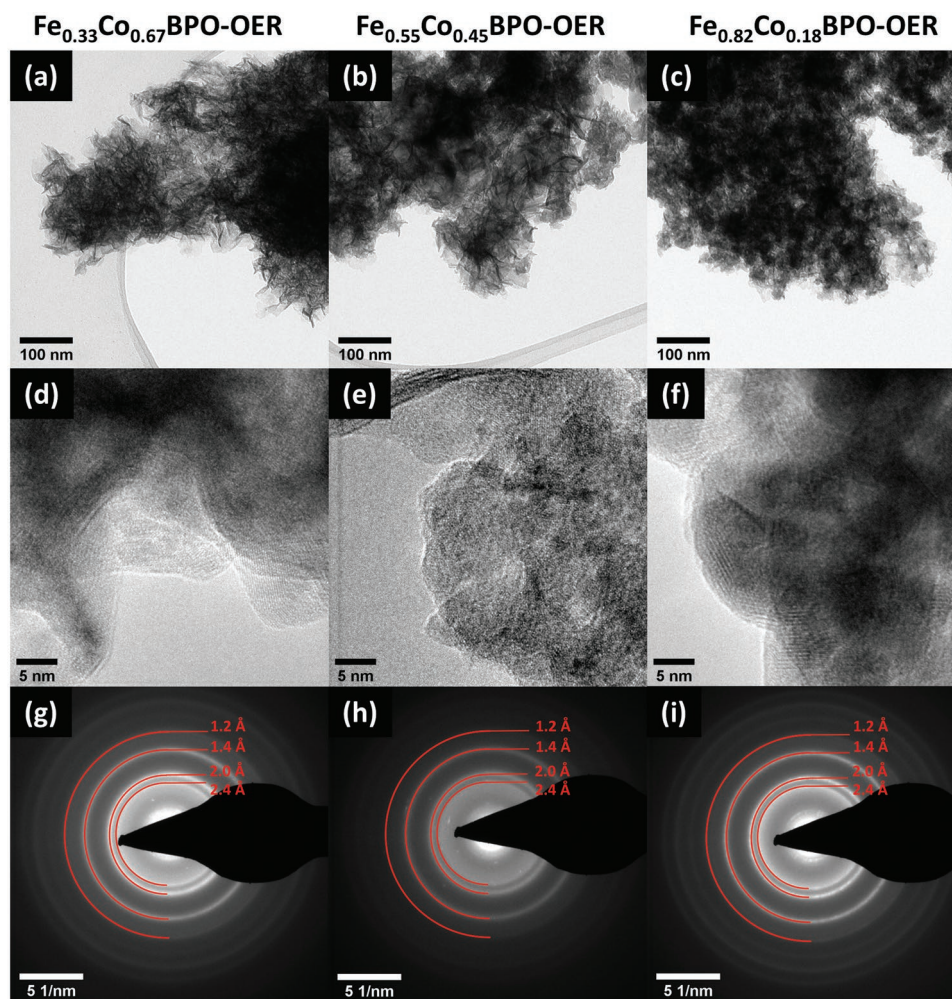
Figure 3. Post-OER samples prepared via CA activation (1.56 V_{RHE}, 2 min) and subsequent CP measurement for 1 h at 25 mA cm^{-2}. TEM images, HR-TEM images, and SAED patterns of samples a,d,g) Fe$_{0.33}$Co$_{0.67}$BPO-OER, b,e,h) Fe$_{0.55}$Co$_{0.45}$BPO-OER, and c,f,i) Fe$_{0.82}$Co$_{0.18}$BPO-OER, respectively. The distances refereeing to the red rings in the SAED indicate the presence of a layered cobalt-iron oxyhydroxide phase.

Tafel slopes for Co(Fe)O$_x$H$_y$ ($\approx$30 mV dec^{-1})[14,62] and indicates a similar active site structure and catalytic mechanism for all three Fe$_{1-x}$Co$_x$BPO samples. CoBPO on the other hand shows a much higher Tafel slope with 47 mV dec^{-1}, which is much closer to the values of Co layered double hydroxide,[63] indicating a different active site structure and mechanism, which is not unexpected, considering the absence of Fe in the material. Furthermore, double-layer capacitance (C_{dl}) measurements did not find significant differences (Figures S15 and S16, Supporting Information), but one should be aware that these measurements are very doubtful due to conductivity limitations, as described in previous reports.[25,51,64,65]

The best-performing catalyst Fe$_{0.55}$Co$_{0.45}$BPO was further tested for its stability during OER. In this regard, a chronopotentiometry (CP) measurement was performed at 10 mA cm^{-2} for 48 h (Figure 2f) demonstrating a stable activity on FTO with only a minor deactivation over time. Overall, the activity trend is very clear where the incorporation of Fe enhances the OER performance, making it an excellent catalyst at the given ratios (Fe$_{0.33}$Co$_{0.67}$BPO and Fe$_{0.55}$Co$_{0.45}$BPO). The pure CoBPO, as well

as a too-high amount of Fe (Fe$_{0.82}$Co$_{0.18}$BPO), leads to a significant decrease in activity.

2.3. Post-OER Characterization

Post-OER samples were prepared by CA activation (1.56 V_{RHE}, 2 min) and subsequent CP measurement for 1 h at 25 mA cm^{-2} under OER conditions. A cross-sectional SEM image of Fe$_{0.55}$Co$_{0.45}$BPO before and after OER demonstrates that the film thickness does not change significantly and remains stable even after OER (Figure S17, Supporting Information). Furthermore, SEM-EDX mapping and the corresponding spectra for the Fe$_{1-x}$Co$_x$BPO-OER samples (Figures S18–S20, Supporting Information) show that the Fe:Co ratio remains similar before and after OER. Oxygen remains throughout the samples. However, the phosphorus content decreased dramatically, caused by leaching. In addition to the complete phosphorus leaching, boron and lithium leached out entirely as well, consistent with the high solubility of phosphate, borate, and Li ions in

the aqueous potassium hydroxide electrolyte. These observations were also confirmed by ICP-OES (Table S1, Supporting Information). Transmission electron microscopy (TEM) in **Figure 3**a–c and high-resolution TEM (Figure 3d–f) images display a sheet-like structure for all Fe$_{1-x}$Co$_x$BPO-OER samples. Furthermore, selected area electron diffraction (SAED) patterns (Figure 3g–i) show rings for all Fe$_{1-x}$Co$_x$BPO-OER samples, demonstrating at least a minimum degree of order of the post-OER samples. The distances of the rings in the SAED at 1.2, 1.4, 2.0, and 2.4 Å, correlate well with the expected layered oxyhydroxide phases.[25] Furthermore, X-ray photoelectron spectroscopy (XPS) was applied to the most active sample Fe$_{0.55}$Co$_{0.45}$BPO and Fe$_{0.55}$Co$_{0.45}$BPO-OER, as shown in Figures S21 and S22, Supporting Information, confirming the drastic surface changes after OER.

Compared to the previously reported CoBPO, which did not fully reconstruct. Herein, all four cobalt and cobalt-iron borophosphates were fully reconstructed,[50] which is most likely caused by the additionally applied ball milling process that efficiently reduced the particle size of borophosphates. In this regard, Kwon et al. have shown that ball milling can activate the sample to fully reconstruct. Furthermore, the fast electrochemical activation process via CA might lead to an enhanced leaching process and faster transformation into the active phase.[25]

2.4. Quasi In Situ X-Ray Absorption Spectroscopy (XAS) Characterization

To identify the electronic state and atomic-scale structure, the disordered cobalt-iron oxyhydroxide phases together with their dynamic response to an OER potential, XAS has been measured. Two potentials were chosen, one is 0.91 V$_{RHE}$ just below the (Figure 2c) redox peaks and the other is at 1.56 V$_{RHE}$ within the OER region. Before any measurement, the Fe$_{1-x}$Co$_x$BPO electrodes were fully reconstructed into oxyhydroxides by a 2 min CA (1.56 V$_{RHE}$) measurement followed by 1 h CP (25 mA cm^{-2}). Subsequently, 0.91 or 1.56 V$_{RHE}$ were applied for 10 min, and the samples freeze quench in liquid

nitrogen at this potential, where the samples remained until their measurement at 20 K in a helium-flow cryostat.

2.4.1. Quasi In Situ X-Ray Absorption Near Edge Structure (XANES)

For each of the four samples, a Co and Fe K-edge spectrum was acquired at the two different potentials. These spectra were used to estimate the bulk oxidation state of the respective transition metals. To do so, the inflection points of the pre-edges of the four cobalt-iron samples together with three cobalt and three iron reference compounds were aligned concerning their energy (Figures S23–S26, Supporting Information). To quantify the K-edge positions, a previously published integral method was used.[66] The K-edge positions and the known oxidation states of the reference compounds were used to deduce a linear relation between the K-edge and oxidation state (Figures S27 and S28, Supporting Information).

Figure 4a shows the resulting transition-metal oxidation states at the two different potentials of the four samples. Consistent with previous reports and the CV of Figure 2c,[25,67] the monometallic cobalt oxyhydroxide sample shows a significant redox activity. At the potential before its redox peaks, the cobalt oxidation state is below 2.9. At the OER potential, the oxidation state is around 3.2, showing the presence of Co^{IV} (or Co$^{(III+\delta)+}$-O$^{(II-\delta)-}$),[27–29] which has been proposed to be a key OER intermediate.[46,67–69] In contrast, the sample with the most iron, Fe$_{0.82}$Co$_{0.18}$BPO-OER, shows no significant change in the cobalt (around 2.9 at 0.91 V$_{RHE}$) or iron (around 2.8 at 1.56 V$_{RHE}$) oxidation state, consistent with the absence of a pronounced redox peak in Figure 2c. This behavior is most likely caused by an insufficient conductivity of oxyhydroxides with predominantly iron.[16] In such a case, only the transition metals in close vicinity to the conducting FTO surface will be electronically wired to the anode and able to change their redox state and participate in electrocatalysis.[16]

For the oxyhydroxides derived from Fe$_{0.33}$Co$_{0.67}$BPO and Fe$_{0.55}$Co$_{0.45}$BPO with intermediate iron-cobalt ratios, the cobalt redox behavior is similar to that of the pure cobalt

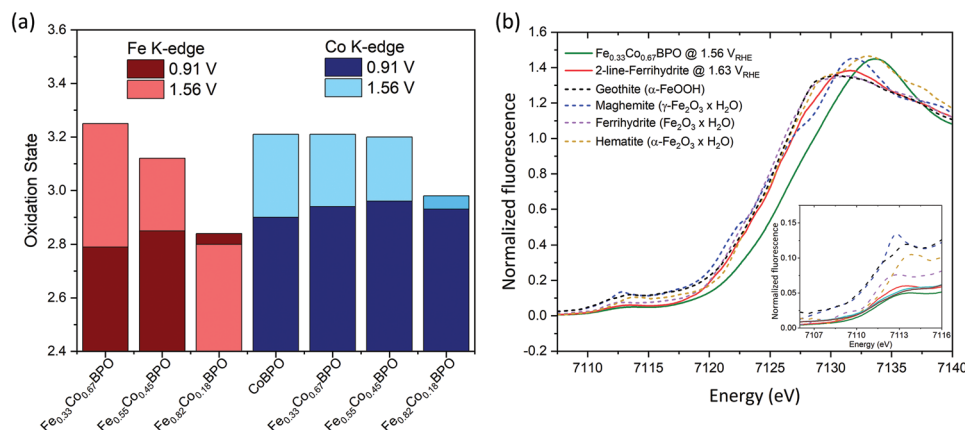**Figure 4.** Quasi in situ XANES measurements of the freeze-quenched reconstructed Fe$_{1-x}$Co$_x$BPO (cobalt-iron oxyhydroxides after reconstruction) samples at two different potentials, before the redox feature (0.91 V$_{RHE}$) and after the redox feature under OER conditions (1.56 V$_{RHE}$). a) Oxidation states determined from the Fe K-edge and Co K-edge. b) Fe K-edge of the Fe$_{0.33}$Co$_{0.67}$BPO (cobalt-iron oxyhydroxide) at 1.56 V$_{RHE}$ compared with different Fe^{III} reference materials; the inset shows the pre-edge region of the Fe K-edge.

sample. Thus, in contrast to nickel-iron oxyhydroxides, where the addition of iron has been shown to inhibit the nickel oxidation,[23,26] for the cobalt-iron oxyhydroxides investigated herein, the cobalt oxidation is not affected by the incorporation of iron and, during OER, it is around 3.2 showing that also Co^{IV} is present. In contrast to the vast majority of previous studies about cobalt-iron oxyhydroxides,[34,46] we observe a pronounced redox activity for iron ranging from Fe^{II} to oxidation states above Fe^{III}. For the $Fe_{0.33}Co_{0.67}$BPO-derived oxyhydroxide, the change in the iron redox state (from around 2.8 to above 3.2) is even larger than the change in the cobalt oxidation state (from around 2.9 to 3.2). XANES is a bulk technique and the approximated oxidation states are average values. In this regard, an oxidation state of 2.8 can quite straightforwardly be assigned to a mixture of ≈20% Fe^{II} and 80% Fe^{III}. For the OER in situ oxidation state of 3.2, it is most likely a combination of mainly iron(III) and higher oxidized species such as iron(IV). However, the presence of even higher oxidation states such as Fe^{VI},[30,31] which has been observed in water-free conditions for nickel-iron oxyhydroxides,[33] cannot be ruled out. To verify the presence of an average iron oxidation state above 3, we prepared a set of $Fe^{III}OOH$ reference compounds and compared their XANES edge with the one of the $Fe_{0.33}Co_{0.67}$ oxyhydroxide under OER conditions (Figure 4b). This shows that the Fe K-edge of $Fe_{0.33}Co_{0.67}$ oxyhydroxide at 1.56 V_{RHE} is indeed shifted to a higher energy than one of all these iron reference compounds of which the 2-line ferrihydrite was also measured in situ under OER conditions with an even higher potential (1.63 V_{RHE}).[70] The observation that

the Fe K-edge has a comparable edge position for various Fe^{III} compounds, even if those are structurally different has also been shown in the literature.[71] Therefore, we conclude that, for the herein investigated cobalt-iron oxyhydroxides, iron indeed has a substantial redox activity and that iron oxidation states above three are present during the OER.

2.4.2. Quasi In Situ Extended X-Ray Absorption Fine Structure (EXAFS)

EXAFS plots of the Co and Fe K-edge spectra of the four samples acquired at the potential before (0.91 V_{RHE}) and after (1.56 V_{RHE}) the redox peaks are shown in Figure 5a,b. The k^3-weighted EXAFS spectra are given in Figures S29 and S30, Supporting Information. All spectra were simulated with a model based on layers of edge-sharing $[MO_6]$ octahedra as they are present in layered double hydroxide and cobalt-iron oxyhydroxides. Such a layer is shown in Figure 5c. The three solid white circles represent the three distances (R) from the central cobalt atom that were considered. The EXAFS peaks are also assigned to the structural motifs in Figure 5d. The number of atoms that are intercepted by the circles (six for each of the three) represents the population (N) that one would expect in a perfectly ordered (single crystal) material with endlessly large layers. For smaller layer (domain) sizes, the number of cobalt/iron atoms at the edges with less than six neighbors increases resulting in lower populations. All EXAFS plots are dominated by two large peaks, of which the second one has a
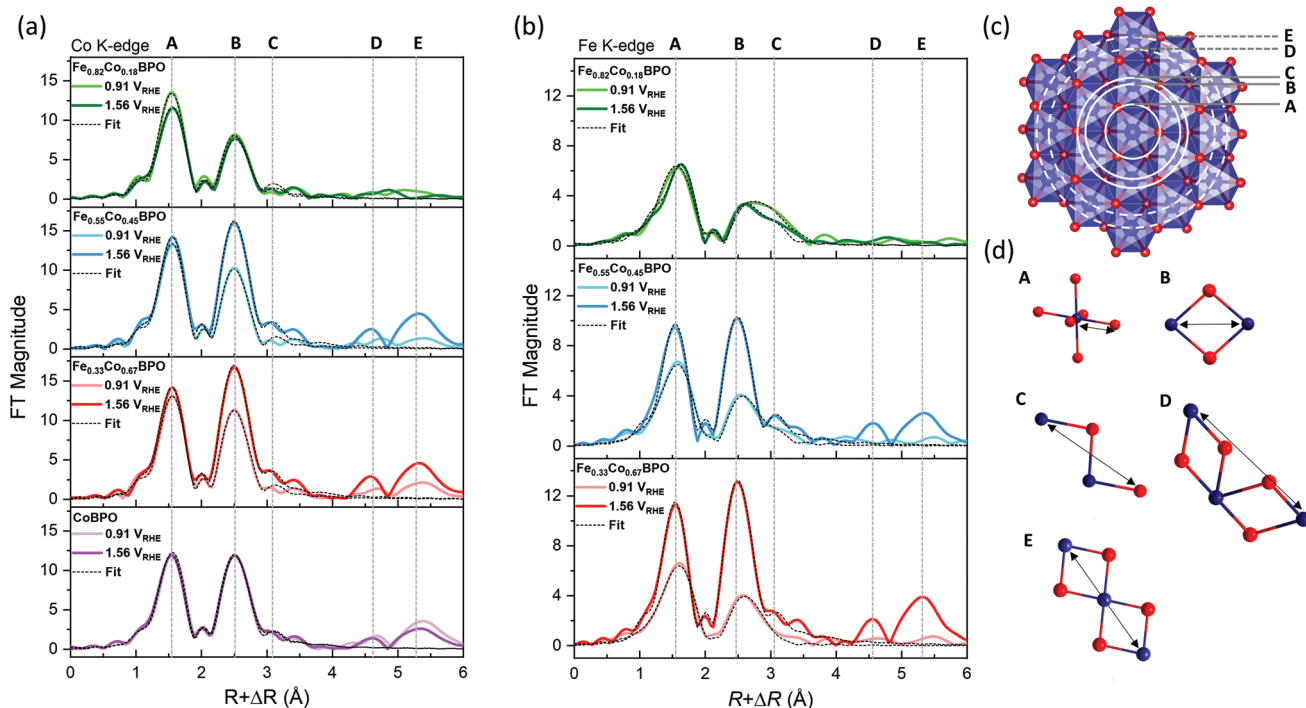

Figure 5. In situ EXAFS data of the freeze-quenched reconstructed $Fe_{1-x}Co_x$BPO samples (cobalt-iron oxyhydroxides after reconstruction) at two different potentials, before the redox feature (0.91 V_{RHE}) and under OER conditions (1.56 V_{RHE}). a) Co K-edge and b) Fe K-edge, with the corresponding fits. c) Structural model of layers of edge-sharing $[MO_6]$ octahedra as present in cobalt-iron oxyhydroxides with the lattice distances (white circles) for the EXAFS coordination shells. d) Structural motifs for the given lattice distances for the EXAFS coordination shells.

**ADVANCED
SCIENCE NEWS**
www.advancedsciencenews.com

**ADVANCED
ENERGY
MATERIALS**
www.advenergymat.de

shoulder on the right. The first peak (A) is assignable to the first circle of our model and thus an M–O bond distance, and the second peak (B) is the M–M distance between the metals of two edge-sharing (or in other words di-μ-oxo bridged) $[MO_6]$ octahedra. The right shoulder of this peak (C) is the M–O distance between the metal center of one $[MO_6]$ octahedra and the oxygen of a neighboring $[MO_6]$ octahedra. The simulations are shown as black lines in Figure 5a,b and the fitting data is given in Tables S2 and S3, Supporting Information. In all cases, they reproduce the experimental data well. Furthermore, for some samples, additional peaks between 4–6 Å can be seen. These peaks, (D) and (E), are the M–M distance to the second nearest neighboring $[MO_6]$ octahedra as marked by the dashed circles in Figure 5c and the models in Figure 5d.[51] These distances were not simulated and will only be discussed qualitatively.

For the sample containing only cobalt, the spectra at the potential before the redox peak and during OER are very similar and the differences in the R and N values of the simulations are small (Table S2, Supporting Information), showing that a layered cobalt oxyhydroxide-like structure is adapted, which persists in the cobalt oxidation state range 2.9–3.2.

For the sample with mainly iron, $Fe_{0.82}Co_{0.18}BPO$, the second peak is substantially less intense than the first one and the peaks in the range of 4–6 Å are barely visible. These characteristics are typical for a lower degree of order and can be observed in the Co and Fe EXAFS plots of reconstructed $Fe_{0.82}Co_{0.18}BPO$ at both potentials and in the Co and Fe EXAFS plots of reconstructed $Fe_{0.33}Co_{0.67}BPO$ and $Fe_{0.55}Co_{0.45}BPO$ at 0.91 V_{RHE}. In these four Fe EXAFS plots, the two main peaks are broader indicating that more than one bond length is present for the Fe–O and Fe–M distance. Indeed, the simulation of these spectra was unsuccessful with only three coordination shells (Table S3, Supporting Information). Therefore, two Fe–O distances and two respective Fe–M distances were used to simulate them, which results in good reproduction of the experimental data. The two Fe–O distances are a short one with around 1.90 Å and a longer one with around 2.04 Å, this automatically results in two different Fe–M distances, of which one is around 2.85 Å and the other around 3.00 Å. Consistently, we also used two Co–M shells to fit the Co EXAFS reconfirming the variation in the Fe-M distances (Table S2, Supporting Information). The four samples with the additional elongated Fe–O bond contain average iron oxidation states below three (around 2.8 in all cases, see Figure 4a). This reduced oxidation state explains the occurrence of an elongated bond (the Fe–O bond distance in $Fe^{II}(OH)_2$ is around 0.1 Å longer than in $Fe^{III}OOH$), and such two different Fe–O bond distances have already been observed previously in cobalt-iron oxyhydroxides and several FeOOH compounds (Table S4, Supporting Information).[46] For all cobalt EXAFS plots, the addition of another, longer Co–O distance did not substantially improve the fits and resulted in unstable fits. Thus, we assume only one distance is present, which is consistent with previous reports[25,51] and a smaller amount of Co^{II} (oxidation state around 2.9) is present compared to Fe^{II} (oxidation state around 2.8).

Most interesting is the structure of the most active samples, reconstructed $Fe_{0.33}Co_{0.67}BPO$ and $Fe_{0.55}Co_{0.45}BPO$, under OER conditions. In contrast to their EXAFS spectra at 0.91 V_{RHE}, the in situ OER EXAFS spectra are well simulated with only

one Co–O and Fe–O bond length. Adding an additional M–O bond length resulted in unstable fits. The Co–O bond length was found to be around 1.89 Å and the Co–M distance around 2.84 Å, which is consistent with bulk-active amorphous cobalt catalysts,[25] the average bond length of Co_4O_4 cubane model compounds under OER conditions,[72] and extrapolations of all surface di-μ_2-oxo cobalt sites under OER conditions.[28] Therefore, we assume that all transition-metal atoms are electronically wired to the anode and have access to the electrolyte, even though a comparably high loading of 130 μg cm^{-2} transition-metal was used. Remarkably, the single Fe–O bond length is identical to the Co-O bond length in these two samples during OER. This is surprising, as Fe^{III}–O bonds in various FeOOH structures comprising $[FeO_6]$ octahedra are usually longer than 2 Å and even compounds containing only $[Fe^{IV}O_6]$ octahedra have average bond distances of around 1.92 Å (see Table S4, Supporting Information for various examples). Thus, the Fe–O bond is substantially contracted in the CoOOH matrix. In our case, another reason for such a short Fe–O bond is probably the presence of Fe^{IV} or the presence of μ-oxyl radicals as bridging anionic species.

3. Discussion

In contrast to our previous study on LiCoBPO, where, even after 24 h, only the near-surface area of the precatalyst was reconstructed into oxyhydroxides, we successfully applied a ball milling procedure in analogy to Kwon et al., which enabled us to fully reconstruct the $LiFe_{1-x}Co_xBPO$ with four different Co:Fe ratios within minutes to cobalt-iron oxyhydroxides.[52] We have previously shown that such reconstruction processes enable the formation of oxyhydroxides with disorderly stacked, relatively small domain sizes, which are electrolyte penetrable and thus to a significant extent bulk-active.[25] As XAS is a bulk technique, this electrolyte penetrability is ideal, as the averaged XAS results mainly yield information on transition-metal centers that could potentially participate in the OER. Our quasi in situ XAS measurements on these samples show that the Co–O bond distances and cobalt oxidation states are comparable to those of bulk-active amorphous cobalt catalysts,[25] extrapolations of all surface di-μ_2-oxo cobalt sites under OER conditions,[28] and the average bond length of Co_4O_4 cubane model compounds under OER conditions,[72] showing that these samples behave comparable to an all-surface structure, due to their electrolyte-penetrability.

The electrocatalytic investigations show that the oxyhydroxide samples with a Fe:Co ratio of 33:67 and 55:45 are the most OER active. The pure cobalt sample's activity is hampered by the absence of iron, which is crucial for fast OER kinetics.[13] The sample with a Fe:Co ratio of 82:18 is insufficiently conducted to enable the participation of many active sites, consistent with previous reports.[13,16,45] We find that the same Tafel slope for all three samples containing cobalt and iron are the same, showing that all of them have the same kind of active sites, which are likely di-μ_2-oxo(/oxyl radical) bridged bimetallic Co-Fe edge sites, as suggested in previous reports.[10,20,46] In this regard, it is reasonable that the sample with an around 50:50 ratio is the most active, as it should have the most bimetallic active sites

assuming a statistical distribution. This assumption is also supported by the redox peak shift, which is most pronounced in that sample, indicating the strongest interaction between iron and cobalt. In contrast to reported nickel-iron oxyhydroxides,[23] we cannot observe a significant decrease of the redox activity through the addition of iron and observe only an anodic shift.

Quasi in situ XAS of the four different cobalt(-iron) oxyhydroxides at a potential (0.91 V_{RHE}) before their redox peak and during OER (1.56 V_{RHE}) revealed a substantial cobalt redox behavior with an oxidation state of around 2.9 below the redox peak and 3.2 at OER conditions. In contrast to various previous investigations,[23,46] we could also observe a redox activity of the iron centers, which was even slightly more pronounced (2.8 to above 3.2) than the one of cobalt. We note that Boettcher and co-workers also identified a shift in the iron edge at a potential just before the OER and during OER, but this shift is smaller than the one observed herein.[40] Furthermore, in contrast to this report, Boettcher and co-workers did not observe any redox activity at the cobalt sites.[40] Most importantly, by comparison to multiple Fe^{III} K-XANES edges, we identify iron in oxidations states above three, which has been proposed to be a crucial part of the active sites in such systems.[23,26,33] These highly oxidized iron species have been challenging to detect, as the rate-determining step has been suggested to be the iron oxidation and that the formed highly oxidized iron species rapidly reacts in the OER reaction.[23,26,33,35] Thus, the iron content during the reaction is minute. We hypothesize that the reason for their detection herein is the following: The investigated cobalt-iron oxyhydroxides are electrolyte penetrable and thus most of the transition metals are anodically wired and have access to the electrolyte for the required proton exchange, needed to undergo redox chemistry (e.g., $Fe^{III}OOH \rightarrow Fe^{IV}O_2 + H^+ + e^-$). However, compared to surface-active materials, electrolyte access is limited by mass transport in parts of the bulk catalyst. Thus, some iron sites are oxidized beyond three but do not have sufficient access to the substrate to rapidly react (it is also possible that the local electrolyte is too acidic due to the proton formation by the iron oxidation and OER). Therefore, they remain in the highly oxidized state for a longer time and can be detected.

Consistent with the high oxidation state of iron, we find an in situ Fe–O bond length that is around 6% shorter than in reported FeOOH compounds. For nickel-iron oxyhydroxides, this contraction of the Fe–O bond has previously been detected by Friebel et al.[56] Furthermore, Boettcher et al. and Yeo et al. also detected bond contractions for cobalt-iron-based materials.[38,40] Herein, this contracted Fe–O bond length is identical to the Co–O one. As the core of the OER is the removal of electrons from oxygen atoms, oxygen redox chemistry at the catalyst's active sites is crucial for its catalysis.[29] Recently, it has been shown that the Co–O bond length observed herein is consistent with a $Co^{III}–O^{\bullet}$ oxyl radical species.[28] As we also observe a similarly short Fe–O bond length, we hypothesize that the cobalt and iron atoms are di-μ_2-oxo bridged by oxyl radical and that these units are the active sites. Furthermore, the bond lengths and M–M distance can be used to calculate the geometry of the $[MO_6]$ octahedra which is shown in **Figure 6**. Consistent with a previous report on nickel-iron oxyhydroxides,[24] it shows a strong distortion.
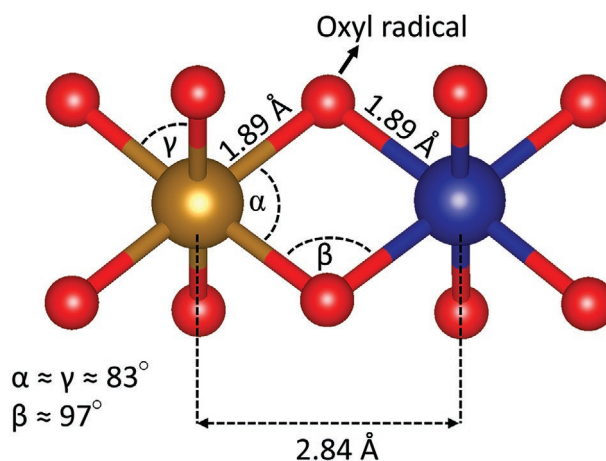

Figure 6. The geometry of a bimetallic Fe–Co site as identified by the EXAFS measurements in the cobalt-iron oxyhydroxides formed through helical borophosphate reconstruction. The Co–O bond distance is consistent with the presence of a μ-oxyl radical.[28] The Fe–O bond distance is around 6% shorter than in oxidic iron(III) compounds, which could be explained by the oxyl radical character of the oxygen. We hypothesize that such oxyl radical bridged bimetallic species are the active centers for OER catalysis.

4. Conclusion

In the present study, we successfully synthesized helical $LiFe_{1-x}Co_x$ borophosphates with four different Co:Fe ratios and applied a ball milling procedure, enabling us to fully reconstruct the material electrochemically within minutes into cobalt-iron oxyhydroxides, which are comparable to an all-surface structure, due to their bulk-activity and electrolyte-penetrability. Electrocatalytic investigations on flat FTO substrates show the highest OER activity for oxyhydroxide samples with a Fe:Co ratio of 33:67 and 55:45, with $\eta_{10} = 277$ mV and $\eta_{10} = 270$ mV, respectively. Iron is crucial for fast OER kinetics, which leads to a decreased activity of the pure cobalt sample. The material with the highest iron content (82:12) suffers from insufficient conductivity and reduced participation of active sites. Still, for all cobalt-iron samples, the same active site structure is observed.

Quasi in situ X-ray absorption spectroscopy was applied to track the redox behavior and to identify the active structure. The quasi in situ XAS measurements of the four different cobalt(-iron) oxyhydroxides before the redox peak (0.91 V_{RHE}) and during OER (1.56 V_{RHE}) demonstrate strong interactions between iron and cobalt correlated to an anodic redox peak shift, without a decrease of the redox activity through the addition of iron. Furthermore, the quasi in situ XAS measurements reveal a substantial cobalt redox behavior. Moreover, in contrast to various previous investigations, a redox activity of the iron centers can be observed with oxidation states up to 3.2. Therefore, we identify iron in oxidation states above three in cobalt-iron oxyhydroxides. This might stem from the presence of Fe^{IV} or even higher oxidation states, which have been proposed to be a crucial part of the active sites in these systems. We believe that the detection of this highly active site is possible herein, due to limited substrate availability in the bulk of the catalyst.

Furthermore, we find a strong distortion of the $[MO_6]$ octahedra and an in situ Fe–O bond length that is around 6% shorter than in reported FeOOH compounds and identical to the one of Co-O during OER. We hypothesize that the short M–O bond length could be caused by the presence of oxyl radical species and that di-μ-oxyl radical bridged bimetallic cobalt iron motifs are the active sites. We believe that our detailed electronic and structural investigation of the active phase in cobalt-iron oxyhydroxides can prove essential for theoretical investigations and design-based catalyst development.

Supporting Information

Supporting Information is available from the Wiley Online Library or from the author.

Acknowledgements

Conflict of Interest

The authors declare no conflict of interest.

Author Contributions

J.N.H. and L.R. contributed equally to this work. P.W.M. and J.N.H. initiated the idea and developed it together with L.R. J.N.H. synthesized the materials. L.R. performed the electrocatalysis experiments and acquired and analyzed all characterization data except transmission electron microscopy, which was acquired by J.N.H., scanning electron microscopy, which was acquired by I.M., and XAS, which was acquired and simulated by S.M. L.R. wrote the results part and the conclusion. J.N.H. wrote the abstract, introduction, XAS part, and discussion. P.W.M., M.D., and H.D. supervised the study. All authors discussed the results and commented on the manuscript.

Data Availability Statement

The data that support the findings of this study are available in the supplementary material of this article.

[1] T. R. Cook, D. K. Dogutan, S. Y. Reece, Y. Surendranath, T. S. Teets, D. G. Nocera, *Chem. Rev.* **2010**, *110*, 6474.

[2] H. B. Gray, *Nat. Chem.* **2009**, *1*, 7.

[3] D. G. Nocera, *Acc. Chem. Res.* **2017**, *50*, 616.

[4] I. Staffell, D. Scamman, A. Velazquez Abad, P. Balcombe, P. E. Dodds, P. Ekins, N. Shah, K. R. Ward, *Energy Environ. Sci.* **2019**, *12*, 463.

[5] M. van der Spek, C. Banet, C. Bauer, P. Gabrielli, W. Goldthorpe, M. Mazzotti, S. T. Munkejord, N. A. Røkke, N. Shah, N. Sunny, D. Sutter, J. M. Trusler, M. Gazzani, *Energy Environ. Sci.* **2022**, *15*, 1034.

[6] I. Roger, M. A. Shipman, M. D. Symes, *Nat. Rev. Chem.* **2017**, *1*, 0003.

[7] N.-T. Suen, S.-F. Hung, Q. Quan, N. Zhang, Y.-J. Xu, H. M. Chen, *Chem. Soc. Rev.* **2017**, *46*, 337.

[8] H. Dau, C. Limberg, T. Reier, M. Risch, S. Roggan, P. Strasser, *ChemCatChem* **2010**, *2*, 724.

[9] J. N. Hausmann, B. Traynor, R. J. Myers, M. Driess, P. W. Menezes, *ACS Energy Lett.* **2021**, *6*, 3567.

[10] F. Dionigi, Z. Zeng, I. Sinev, T. Merzdorf, S. Deshpande, M. B. Lopez, S. Kunze, I. Zegkinoglou, H. Sarodnik, D. Fan, A. Bergmann, J. Drnec, J. F. de Araujo, M. Gliech, D. Teschner, J. Zhu, W.-X. Li, J. Greeley, B. R. Cuenya, P. Strasser, *Nat. Commun.* **2020**, *11*, 2522.

[11] B. R. Wygant, K. Kawashima, C. B. Mullins, *ACS Energy Lett.* **2018**, *3*, 2956.

[12] L. Trotochaud, S. L. Young, J. K. Ranney, S. W. Boettcher, *J. Am. Chem. Soc.* **2014**, *136*, 6744.

[13] M. S. Burke, M. G. Kast, L. Trotochaud, A. M. Smith, S. W. Boettcher, *J. Am. Chem. Soc.* **2015**, *137*, 3638.

[14] M. S. Burke, L. J. Enman, A. S. Batchellor, S. Zou, S. W. Boettcher, *Chem. Mater.* **2015**, *27*, 7549.

[15] D. Y. Chung, P. P. Lopes, P. Farinazzo Bergamo Dias Martins, H. He, T. Kawaguchi, P. Zapol, H. You, D. Tripkovic, D. Strmcnik, Y. Zhu, S. Seifert, S. Lee, V. R. Stamenkovic, N. M. Markovic, *Nat. Energy* **2020**, *5*, 222.

[16] S. Zou, M. S. Burke, M. G. Kast, J. Fan, N. Danilovic, S. W. Boettcher, *Chem. Mater.* **2015**, *27*, 8011.

[17] S. Anantharaj, S. Kundu, S. Noda, *Nano Energy* **2021**, *80*, 105514.

[18] M. S. Burke, S. Zou, L. J. Enman, J. E. Kellon, C. A. Gabor, E. Pledger, S. W. Boettcher, *J. Phys. Chem. Lett.* **2015**, *6*, 3737.

[19] N. Li, D. K. Bediako, R. G. Hadt, D. Hayes, T. J. Kempa, F. von Cube, D. C. Bell, L. X. Chen, D. G. Nocera, *Proc. Natl. Acad. Sci U. S. A.* **2017**, *114*, 1486.

[20] F. Dionigi, J. Zhu, Z. Zeng, T. Merzdorf, H. Sarodnik, M. Gliech, L. Pan, W.-X. Li, J. Greeley, P. Strasser, *Angew. Chem., Int. Ed.* **2021**, *60*, 14446.

[21] G. Młynarek, M. Paszkiewicz, A. Radniecka, *J. Appl. Electrochem.* **1984**, *14*, 145.

[22] M. B. Stevens, C. D. M. Trang, L. J. Enman, J. Deng, S. W. Boettcher, *J. Am. Chem. Soc.* **2017**, *139*, 11361.

[23] M. Görlin, P. Chernev, J. Ferreira de Araújo, T. Reier, S. Dresp, B. Paul, R. Krähnert, H. Dau, P. Strasser, *J. Am. Chem. Soc.* **2016**, *138*, 5603.

[24] R. D. L. Smith, C. Pasquini, S. Loos, P. Chernev, K. Klingan, P. Kubella, M. R. Mohammadi, D. González-Flores, H. Dau, *Energy Environ. Sci.* **2018**, *11*, 2476.

[25] J. N. Hausmann, S. Mebs, K. Laun, I. Zebger, H. Dau, P. W. Menezes, M. Driess, *Energy Environ. Sci.* **2020**, *13*, 3607.

[26] M. Görlin, J. Ferreira de Araújo, H. Schmies, D. Bernsmeier, S. Dresp, M. Gliech, Z. Jusys, P. Chernev, R. Kraehnert, H. Dau, P. Strasser, *J. Am. Chem. Soc.* **2017**, *139*, 2070.

[27] D. Drevon, M. Görlin, P. Chernev, L. Xi, H. Dau, K. M. Lange, *Sci. Rep.* **2019**, *9*, 1532.

[28] F. T. Haase, A. Bergmann, T. E. Jones, J. Timoshenko, A. Herzog, H. S. Jeon, C. Rettenmaier, B. R. Cuenya, *Nat. Energy* **2022**, *7*, 765.

[29] H. N. Nong, L. J. Falling, A. Bergmann, M. Klingenhof, H. P. Tran, C. Spöri, R. Mom, J. Timoshenko, G. Zichittella, A. Knop-Gericke, S. Piccinin, J. Pérez-Ramírez, B. R. Cuenya, R. Schlögl, P. Strasser, D. Teschner, T. E. Jones, *Nature* **2020**, *587*, 408.

[30] S. Lee, A. Moysiadou, Y. C. Chu, H. M. Chen, X. Hu, *Energy Environ. Sci.* **2022**, *15*, 206.

[31] N. Li, R. G. Hadt, D. Hayes, L. X. Chen, D. G. Nocera, *Nat. Commun.* **2021**, *12*, 4218.

[32] J. Y. C. Chen, L. Dang, H. Liang, W. Bi, J. B. Gerken, S. Jin, E. E. Alp, S. S. Stahl, *J. Am. Chem. Soc.* **2015**, *137*, 15090.

[33] B. M. Hunter, N. B. Thompson, A. M. Müller, G. R. Rossman, M. G. Hill, J. R. Winkler, H. B. Gray, *Joule* **2018**, *2*, 747.

[34] K. Bhattacharyya, A. A. Auer, *J. Phys. Chem. C* **2022**, *126*, 18623.

[35] H. B. Tao, Y. Xu, X. Huang, J. Chen, L. Pei, J. Zhang, J. G. Chen, B. Liu, *Joule* **2019**, *3*, 1498.

[36] S. Loos, I. Zaharieva, P. Chernev, A. Lißner, H. Dau, *ChemSusChem* **2019**, *12*, 1966.

[37] L. Francàs, S. Corby, S. Selim, D. Lee, C. A. Mesa, R. Godin, E. Pastor, I. E. L. Stephens, K.-S. Choi, J. R. Durrant, *Nat. Commun.* **2019**, *10*, 5208.

[38] L. Gong, X. Y. E. Chng, Y. Du, S. Xi, B. S. Yeo, *ACS Catal.* **2018**, *8*, 807.

[39] B.-J. Kim, E. Fabbri, D. F. Abbott, X. Cheng, A. H. Clark, M. Nachtegaal, M. Borlaf, I. E. Castelli, T. Graule, T. J. Schmidt, *J. Am. Chem. Soc.* **2019**, *141*, 5231.

[40] L. J. Enman, M. B. Stevens, M. H. Dahan, M. R. Nellist, M. C. Toroker, S. W. Boettcher, *Angew. Chem., Int. Ed.* **2018**, *130*, 13022.

[41] S. Lee, L. Bai, X. Hu, *Angew. Chem., Int. Ed.* **2020**, *132*, 8149.

[42] E. Budiyanto, S. Salamon, Y. Wang, H. Wende, H. Tüysüz, *JACS Au* **2022**, *2*, 697.

[43] H. Jin, S. Mao, G. Zhan, F. Xu, X. Bao, Y. Wang, *J. Mater. Chem. A* **2017**, *5*, 1078.

[44] C. Xue, G. Li, J. Wang, Y. Wang, L. Li, *Electrochim. Acta* **2018**, *280*, 1.

[45] K. Sliozberg, Y. Aniskevich, U. Kayran, J. Masa, W. Schuhmann, *Z. Phys. Chem.* **2020**, *234*, 995.

[46] R. D. L. Smith, C. Pasquini, S. Loos, P. Chernev, K. Klingan, P. Kubella, M. R. Mohammadi, D. Gonzalez-Flores, H. Dau, *Nat. Commun.* **2017**, *8*, 2022.

[47] X. Liu, J. Meng, J. Zhu, M. Huang, B. Wen, R. Guo, L. Mai, *Adv. Mater.* **2021**, *33*, 2007344.

[48] J. N. Hausmann, P. W. Menezes, *Curr. Opin. Electrochem.* **2022**, *34*, 100991.

[49] P. W. Menezes, C. Walter, B. Chakraborty, J. N. Hausmann, I. Zaharieva, A. Frick, E. von Hauff, H. Dau, M. Driess, *Adv. Mater.* **2021**, *33*, 2004098.

[50] P. W. Menezes, A. Indra, I. Zaharieva, C. Walter, S. Loos, S. Hoffmann, R. Schlögl, H. Dau, M. Driess, *Energy Environ. Sci.* **2019**, *12*, 988.

[51] J. N. Hausmann, S. Mebs, H. Dau, M. Driess, P. W. Menezes, *Adv. Mater.* **2022**, *34*, 2207494.

[52] J. Kwon, H. Han, S. Jo, S. Choi, K. Y. Chung, G. Ali, K. Park, U. Paik, T. Song, *Adv. Energy Mater.* **2021**, *11*, 2100624.

[53] R. Kniep, H. G. Will, I. Boy, C. Röhr, *Angew. Chem., Int. Ed.* **1997**, *109*, 1052.

[54] P. W. Menezes, S. Hoffmann, Y. Prots, R. Kniep, Z. Kristallogr., *Z. Kristallogr. – New Cryst. Struct.* **2008**, *223*, 333.

[55] P. W. Menezes, C. Panda, C. Walter, M. Schwarze, M. Driess, *Adv. Funct. Mater.* **2019**, *29*, 1808632.

[56] D. Friebel, M. W. Louie, M. Bajdich, K. E. Sanwald, Y. Cai, A. M. Wise, M.-J. Cheng, D. Sokaras, T.-C. Weng, R. Alonso-Mori, R. C. Davis, J. R. Bargar, J. K. Nørskov, A. Nilsson, A. T. Bell, *J. Am. Chem. Soc.* **2015**, *137*, 1305.

[57] L. Gao, X. Cui, C. D. Sewell, J. Li, Z. Lin, *Chem. Soc. Rev.* **2021**, *50*, 8428.

[58] L. Han, S. Dong, E. Wang, *Adv. Mater.* **2016**, *28*, 9266.

[59] F. Lyu, Q. Wang, S. M. Choi, Y. Yin, *Small* **2019**, *15*, 1804201.

[60] M. Yu, E. Budiyanto, H. Tüysüz, *Angew. Chem., Int. Ed.* **2022**, *61*, 202103824.

[61] S. Anantharaj, S. Noda, M. Driess, P. W. Menezes, *ACS Energy Lett.* **2021**, *6*, 1607.

[62] R. D. L. Smith, M. S. Prévot, R. D. Fagan, Z. Zhang, P. A. Sedach, M. K. J. Siu, S. Trudel, C. P. Berlinguette, *Science* **2013**, *340*, 60.

[63] F. Song, X. Hu, *Nat. Commun.* **2014**, *5*, 4477.

[64] F. Dionigi, J. Zhu, Z. Zeng, T. Merzdorf, H. Sarodnik, M. Gliech, L. Pan, W.-X. Li, J. Greeley, P. Strasser, *Angew. Chem., Int. Ed.* **2021**, *133*, 14567.

[65] A. S. Batchellor, S. W. Boettcher, *ACS Catal.* **2015**, *5*, 6680.

[66] H. Dau, P. Liebisch, M. Haumann, *Anal. Bioanal. Chem.* **2003**, *376*, 562.

[67] M. Risch, F. Ringleb, M. Kohlhoff, P. Bogdanoff, P. Chernev, I. Zaharieva, H. Dau, *Energy Environ. Sci.* **2015**, *8*, 661.

[68] A. Moysiadou, S. Lee, C.-S. Hsu, H. M. Chen, X. Hu, *J. Am. Chem. Soc.* **2020**, *142*, 11901.

[69] M. Zhang, M. de Respinis, H. Frei, *Nat. Chem.* **2014**, *6*, 362.

[70] R. Beltrán-Suito, V. Forstner, J. N. Hausmann, S. Mebs, J. Schmidt, I. Zaharieva, K. Laun, I. Zebger, H. Dau, P. W. Menezes, M. Driess, *Chem. Sci.* **2020**, *11*, 11834.

[71] S. Neiser, D. Rentsch, U. Dippon, A. Kappler, P. G. Weidler, J. Göttlicher, R. Steininger, M. Wilhelm, M. Braitsch, F. Funk, E. Philipp, S. Burckhardt, *BioMetals* **2015**, *28*, 615.

[72] F. Song, R. Moré, M. Schilling, G. Smolentsev, N. Azzaroli, T. Fox, S. Luber, G. R. Patzke, *J. Am. Chem. Soc.* **2017**, *139*, 14198.